Nanoscale

Accepted Manuscript

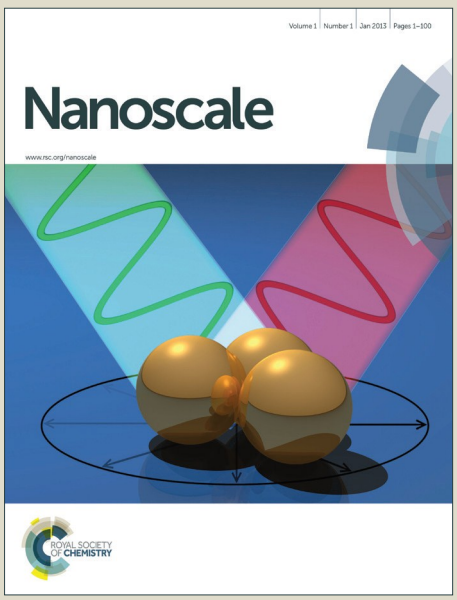

ROYAL SOCIETY OF CHEMISTRY

www.rsc.org/nanoscale

Journal Name

RSCPublishing

ARTICLE

Self-Assembled Organic Hexagonal Micro-prisms with High Second Harmonic Generation Efficiency for Photonic Devices

Cite this: DOI: 10.1039/x0xx00000x

Received 00th January 2012,
Accepted 00th January 2012

DOI: 10.1039/x0xx00000x

www.rsc.org/

Haihua Zhang, [a] Qing Liao,[*,a] Xuedong Wang,[b] Zhenzhen Xu, [a] Hongbing Fu[*,a,b]

Multiwavelength coherent light sources are key components for circuit integration of nanophotonics. Here, we demonstrated highly efficient second harmonic generation (SHG) in single-crystalline hexagonal micro-prisms (HMPs) of 3-methyl-4-methoxy-4'-nitrostilbene (MMONS) prepared via a facile self-assembled method. We found that the SHG conversion efficiency (η_{SHG}) of MMONS HMPs increases with increasing the prism side length (d). Local electric field $|E|^2$ calculations suggest that the symmetrical hexagonal prism shape of HMPs support helically propagating modes. And the SHG light produced at one end of HMP can be coupled into whispering-gallery (WG) like optical modes with a coupling efficiency of 50~80% and helically propagates along the length of HMPs toward another end. Based on this unique helical propagation of SHG light, we construct an optical interconnector by placing a single MMONS HMP on the top of a single micro-ribbon of 1,2-diphenyl-2-pyrazoline (DP). These easily fabricated MMONS HMPs can act as a coherent source, which adds a key component to the tool box of organic nano- and micro-structure optoelectronics.

Introduction

Coherent light sources of nano- and micro-scale dimensions are key components for circuit integration of nanophotonics, which may find applications ranging from optical signal processing to medical diagnostic.[1,2] Semiconductor nanowire nanolasers had been widely investigated because of its small footprint of devices.[3] The optically flat end-faces of nanowires function as two reflectors of a Fabry-Pérot microcavity along the nanowire length, leading to strong optical confinement. Note that the lasing wavelengths of nanowire nanolasers are determined by the semiconductor constituents, for example, ZnO for ultraviolet output,[4] GaN for visible light,[5] and GaAs for near-infrared region.[6] Therefore, integration of nanowire nanolasers lasing at multiple wavelengths is highly difficult. Second harmonic generation (SHG), in which two low-energy incident photons (ω) combine to one high-energy photon (2ω), provides a possible way to obtain multiple wavelength coherent sources by frequency conversion.[7,8] In particular, SHG in ZnO,[9] GaN,[10] BBO (β-BaB_2O_4)[11] and $KNbO_3$[12,13] nanowires had been recently demonstrated. For future use of these nanowires as local noninvasive light sources, efficient waveguiding of SH signal through nanowires is highly desirable for delivering SH light into different channels of a photonic circuit, but remains largely unexplored.

As compared with their inorganic counterparts, organic semiconductors have several inherent advantages, such as low-cost, low-temperature processing, and compatibility with plastic substrates.[14] Furthermore, the high optical cross-sections, large and ultrafast nonlinear optical (NLO) responses, and broad spectral tenability of organic semiconductors make them attractive in photonic applications.[15] Recently, optical wave-guiding and lasing action had been realized in organic nanowires of polymeric and π-conjugated semiconductors.[16] However, investigation of NLO properties of organic nanostructures had met with limited successes. For example, Xu and co-workers reported strong NLO phenomena of both SHG and two-photon fluorescence (TPF) in microfibers of 2,7-diphenyl-9*H*-fluoren-9-one (DPFO), and observed non-propagation and propagation behaviours for SHG and TPF signals, respectively.[17] Isakov and co-workers demonstrated strong enhancement of SHG in electrospun microfibers of 2-methyl-4-nitroaniline nanocrystals embedded into a matrix of poly(L-lactic acid). [18]

As a promising organic nonlinear optical material, 3-methyl-4-methoxy-4′-nitrostilbene (MMONS) has been widely investigated. The nonlinear optical coefficients d_{33} = 184 pm/V and 195 pm/V were reported for bulk crystal and films correspondingly. [19,20] The SHG efficiency as large as 1250 times of that of urea was only reported for powder samples.[21]

Nonetheless, Here, we report highly efficient SHG in single-crystalline hexagonal micro-prisms (HMPs) of MMONS prepared via a facile self-assembled method. The SHG conversion efficiency (η_{SHG}) of MMONS HMPs was found to increase with increasing the prism side length (d) and reaches a maximum of η_{SHG} = 8.3 ± 0.5% for HMP with d = 2.5 μm, comparable to that of β-BaB_2O_4 microwire. Local electric field $|E|^2$ calculations suggest that the symmetrical hexagonal prism shape of HMPs support helically propagating modes. And the SHG light produced at one end of HMP can be coupled into whispering-gallery (WG) like optical modes with a coupling efficiency of 50~80% and helically propagates along the length of HMPs toward another end. Based on this unique helical propagation of SHG light, we construct an optical interconnector by placing a single MMONS HMP on the top of a single micro-ribbon of 1,2-diphenyl-2-pyrazoline (DP). [22,23] These easily fabricated MMONS HMPs can act as a coherent source, which adds a key component to the tool box of organic nano- and micro-structure optoelectronics, demonstrating the possibility of utilization of MMONS HMPs for future on-chip integration.

Experimental methods

The compound of MMONS used in this study was synthesized according to literatures.[19] In our experiment, MMONS HMPs were prepared via a liquid-phase self-assembling method.[24,25] In brief, a stock solution of MMONS (12.5 mM) in tetrahydrofuran (THF) was pre-prepared. Then 50 μL of this solution was rapidly injected into 1.0 mL of a mixture of deionized water and methanol (volume ratio, v:v = 2:3) at room temperature under shaking. After aging at room temperature for 3 hours, large amount of MMONS HMPs were obtained. Finally, precipitate was centrifugally separated from the colloidal suspension and washed twice using water prior to vacuum drying.

The morphologies and sizes of MMONS HMPs were examined using field emission scanning electron microscopy (FESEM, Hitachi S-4300) at acceleration voltages of 10-15 kV. Prior to analysis, the samples were coated with a thin platinum layer using an Edwards Sputter Coater. Transmission electron microscopy (TEM) images were obtained by a JEOL JEM-1011. One drop of the as-prepared colloidal dispersion was deposited on a carbon-coated copper grid, and dried under high vacuum. TEM measurement was performed at room temperature at an accelerating voltage of 100 kV.

MMONS HMPs was investigated at room temperature in air by a home-made optical microscopy equipped with a 50 × 0.9 NA excitation objective The samples were prepared by placing a drop of dispersion onto a cleaned quartz slide.The excitation laser pulses (800-1200 nm) for the SHG experiment were supplied by an optical parametric amplifier (OPA-800CF, Spectra Physics), which was pumped by the output from a regenerative amplifier (Spitfire, Spectra Physics). The output laser pulse was then focused to a 1.5-μm-diameter spot to pump the selected individual HMP. The micro-area photoluminescence (μ-PL) images were recorded by using a CCD (DVC-1412AM high-resolution digital camera) in a reflective mode. Then μ-PL spectra were collected underneath by using another 50 × 0.9 NA objective that was mounted a 3D movable stage. Finally the collected μ-PL was coupled to an optical fiber and detected using a liquid-nitrogen-cooled CCD (SPEC-10:100BR, Roper Scientific) attached to a polychromator (Spectropro-550i, Acton). The spectral resolution is 0.1 nm. If necessary, we could record the spatially resolved PL spectra along the body of the selected MMONS HMP with a spatial resolution about 1 μm.

The SHG efficiency of MMONS HMPs is defined as $\eta_{SHG} = I(2\omega)/I(\omega)$, where $I(\omega)$ and $I(2\omega)$ are intensities of the fundamental frequency input(1050nm) and the SHG signal(525nm). $I(\omega)$ was recorded directly underneath the bare quartz substrate without sample, while $I(2\omega)$ was recorded underneath the HMP and the substrate. And both intensities had been calibrated by the influence of the quantum efficiency of the CCD.

Results and discussions

Figure 1a depicts a typical scanning electron microscope (SEM) image of as-prepared MMONS HMPs. The hexagonally shaped cross-section could be observed clearly from a vertically grown HMP as shown in the upper-left of Figure 1a. Moreover, it can be seen that well-faceted MMONS HMPs have an edge length of d = 1.6–2.5 μm and a length of l = 6–15 μm (Figure S1), and exhibit smooth outer surfaces. We measured selected area electron diffraction (SAED) pattern (inset of Figure 1b) by directing the electron beam almost perpendicular to the flat top

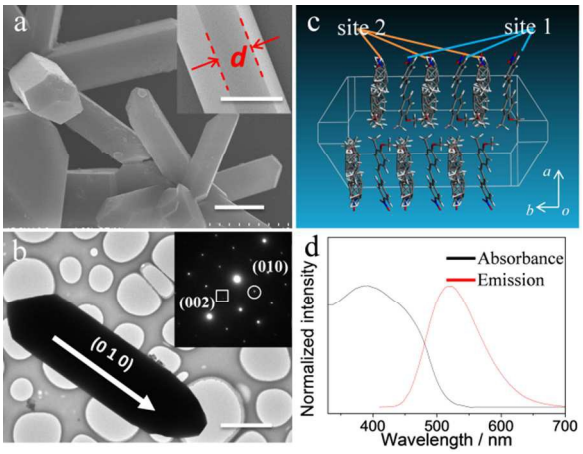

Figure 1. a) SEM images of typical MMONS HMPs. Inset shows a single HMP with an edge length of *d*. Scale bars are 3 μm. (b) TEM image of a single HMP and corresponding SAED pattern (inset). Scale bar is 3 μm. (c) Packing arrangement of MMONS molecules driven by strong π-π stacking along the crystal *b*-axis in theoretically predicted growth morphology. (d) UV–vis absorption (black) and photoluminescence (PL) (red) spectra of MMONS HMPs.

surface of a single HMP (Figure 1b). It had been reported that MMONS crystals have three polymorphs: two orthorhombic forms (CCDC No.658143, 658145) and one monoclinic form

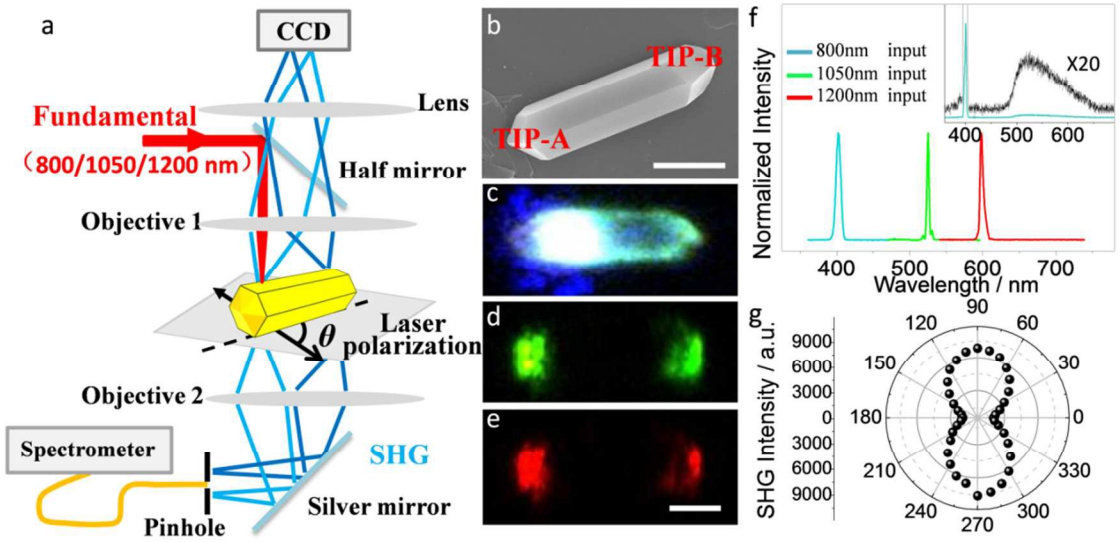

Figure 2. Nonlinear optical responses of MMONS HMPs. (a) Scheme of the experimental setup used for characterizing HMPs SHG effects. Insert: ϑ refers to the angle between the fundamental frequency laser polarization and the long axis of HMP. (b) ~ (e) SEM image and μ-PL images pumped at TIP-A of a single HMP in $\lambda_{fundamental}$ = 800, 1050, 1200nm, respectively. Clearly waveguides of SHG signals are observed. Scale bar is 5 μm. (f) μ-PL spectra recorded at the pump spot when the fundamental frequency laser switched from 800nm, to 1050nm, and to 1200nm, normalized by the intensity of the SHG signal. Insert: the whole spectra when pumped at wavelength of 800nm. (g) Polar plots of the SHG signals as a function of the polarization angle θ shown in (a).

(CCDC No.658144).[26] Especially, the monoclinic form crystallizes in the polar non-centrosymmetric space group $P2_1$ with cell parameters of a = 11.8890 Å, b = 7.41180 Å, c = 15.6083 Å, $\alpha = \gamma$ =90°, and β = 103.661°, and Z = 4. The circled and squared sets of SAED spots in Figure 1b correspond to interplanar spacing values of 7.3 and 7.8 Å, due to Bragg reflections from (010) and (002) crystal planes of non-centrosymmetric monoclinic phase, respectively. The rectangular symmetry of SAED spots clarifies that our HMPs are single crystals. Correlation of SAED pattern to the orientation of the HMP measured makes it clear that single-crystalline HMPs are grown preferentially along the crystal *b*-axis (also see Figure 1b).

To understand the molecular packing, we calculated the equilibrium shape of monoclinic crystal of MMONS for minimum total surface energy by using the software of Material Studio package. The predicted morphology is also a hexagonal prism (Figure S2), similar to MMONS HMPs obtained in our experiment (Figure 1a). This further confirms our assignment of MMONS HMPs to the polar non-centrosymmetric space group $P2_1$. Figure 1c presents a π-π stacking arrangement of MMONS molecules along the crystal *b*-axis, i.e., the length direction of HMPs. Note that MMONS molecule at site 1 is ordered, whereas site 2 exhibits disordered and is occupied by two different conformers.[26] In any event, all MMONS molecules are almost planar and stack perpendicular to the HMP length-direction with their long-axis tilted at an angle about 44° with respect to the substrate. It is known that as an common NLO phenomenon, SHG in organic materials requires a high molecular hyperpolarizability thus a high second-order susceptibility χ(2) together with a non-centrosymmetric molecular organization in the solid state.[27,28] MMONS molecules have an large dipole moment of 5.2 D.[29] This, plus the polar non-centrosymmetric P21 packing, makes MMONS HMPs attractive in SHG application.

To characterize SHG properties of single HMPs, we used a home-built femotosecond-laser scanning microscope. It can be seen from Figure 2a that femtosecond pulses ($\lambda_{fundamental}$, 1 kHz, pulse width 150 fs) from an optical parametric oscillator pumped by a Ti: sapphire regenerative amplifier was used as the fundamental frequency laser and was focused to a 1.5-μm-diameter spot on the tip of HMPs placed on a 3D movable sample stage. The micro-area photoluminescence (μ-PL) image was recorded in a reflective mode using a CCD. And the μ-PL spectra were collected underneath by using another 3D-movable objective 2 coupled to an optical fiber and detected using a liquid-nitrogen cooled charge-coupled device (CCD). To study the coupling efficiency of MMONS HMPs and the optical interconnector feasibility at last, the spatially resolved PL spectra along the body of the selected HMP with a spatial resolution about 1μm could be recorded by adding a pinhole in front of optical fiber.

Figure 2b shows the SEM image of a single HMP with d = 1.9 μm and l = 14.6 μm, while Figure 2c, d and e are corresponding μ-PL images of the same HMP pumped at $\lambda_{fundamental}$ = 800, 1050, 1200 nm, respectively. Remarkably, blue-greenish (Figure 2c), greenish (Figure 2d) and reddish(Figure 2e) μ-PL colors are observed when the fundamental frequency laser switched from 800 nm, to 1050 nm, and to 1200 nm. Figure 2f show the μ-PL spectra recorded at the pump spot. Three sharp bands at 400, 525, and 600nm were observed at half the pump wavelength of $\lambda_{fundamental}$ = 800,

1050, 1200 nm, respectively. This confirms that MMONS HMPs exhibit outstanding SHG properties. Note that under conditions of $\lambda_{fundamental}$ = 800 nm, besides the SHG signal at 400 nm, a PL band from 500 nm to 600 nm with a maximum at 520nm was also observed (see the inset of Figure 2f), which is in good agreement with the PL spectrum of a random mat of HMPs excited at 390 nm (Figure 1d). As shown in Figure 1d, the absorption spectrum of HMPs is a broad peak from 300 to 500 nm centered at 390 nm. Therefore, under conditions of $\lambda_{fundamental}$ = 800 nm, the 400-nm SHG photon produced by frequency upconversion can be partly re-absorbed by MMONS molecules,[30,31] which then emit the green PL at 520 nm. In the sharp contrast, SHG signals at 525 and 600 nm cannot be absorbed by MMONS PL in these cases.

We found that the SHG process in MMONS HMPs is strongly polarization-dependent, due to the well-oriented dipole moment of MMONS along the line joining the acceptor nitro group to the donor methoxyl (Figure S2a inset). Figure 2g show

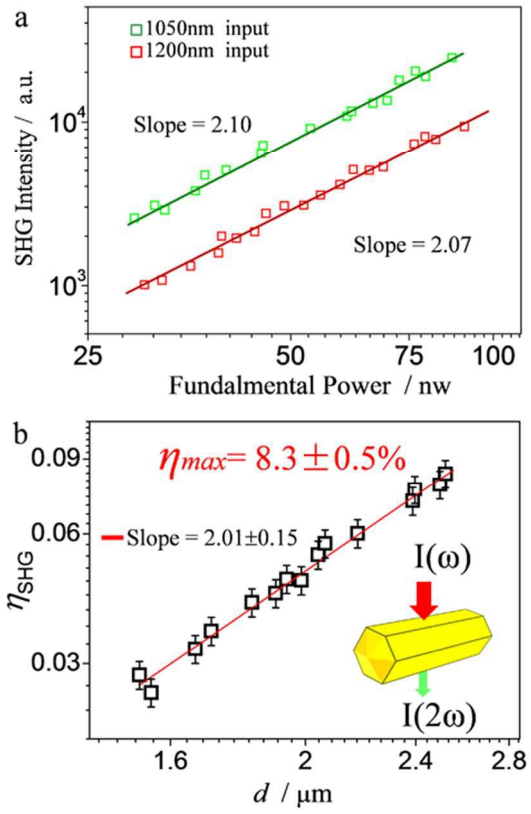

Figure 3. (a) Logarithmic plots of the power dependence of SHG pumped at 1050 nm (green) and 1200 nm (red). (b) Logarithmic plots of the edge length (*d*) dependence of η_{SHG} pumped by 1050-nm fundamental laser. The highest η_{SHG} is 8.3 ± 0.5%. Insert: Schematic representation of the Fundamental frequency laser and second harmonics.

the intensity of SHG = 525 nm (I_{SHG}) as a function of the polarization angle θ between the HMP-length direction (the crystal *b*-axis) and the polarization of the 1050 nm fundamental laser, which was adjusted by a 1/2-λ plate. It can be seen from Figure 2g that I_{SHG} oscillates with a period of 180°between the maximum at θ = 90° or θ = 270° and the minimum at θ = 0° or θ = 180°, with a high polarization ratio[$\rho = (I_{max}-I_{min})/(I_{max}+I_{min})$] of 0.916 ± 0.03. As above mentioned, the dipole moment of MMONS is almost perpendicular to the length direction of HMPs (Figure 1b). Therefore, the maximum SHG was observed at θ = 90° or 270°, when the 1050 nm fundamental laser polarization was parallel to the dipole moment of MMONS molecules. In contrast, when the 1050 nm fundamental laser polarization was perpendicular to the dipole moment of MMONS molecules, the minimum SHG was obtained at θ = 0° or 180°.

By fixing θ = 90°, we further measured the power dependence of SHG intensity as a function of pump power of the fundamental laser. It can be seen from Figure 3a that the SHG intensity scale quadratically with the power of both 1050 nm (green) and 1200 nm (red) femtosecond laser, confirming the two-photon origin of these SHG processes. To understand the influence of HMP size on SHG, quantitative efficiency of SHG was measured by using 1050 nm fundamental with a pump fluence of 80 nJ/cm^2 and θ = 90°. As shown in the inset of Figure 3b, we defined the SHG efficiency, $\eta_{SHG} = I(2\omega)/I(\omega)$, where $I(\omega)$ and $I(2\omega)$ are intensities of the fundamental frequency input and the SHG signal. In our case, we optimized the maximum in SHG intensity by ensuring the fundemental laser perpendicular to MMONS, and fixing θ = 90° (maximum of SHG intensity in polarization dependent) to ensure the maximum in SHG intensity. We investigated a number of individual HMPs. Figure 3b presents the logarithmic plots of η_{SHG} versus d = 1.6–2.5 μm. The value of η_{SHG} increases with increasing the value of d, and reaches a maximum of η_{SHG} = 8.3 ± 0.5% for d = 2.5 μm. Theoretically, η_{SHG} can be expressed by equation,[18]

$$I_{2\omega} \propto n^2\langle\beta^2\rangle(I_\omega)^2 \qquad (1)$$

$$\eta_{SHG} = \frac{I_{2\omega}}{I_\omega} \propto n^2\langle\beta^2\rangle I_\omega \qquad (2)$$

where β is tensor component of second order nonlinear susceptibility and depended on different NLO materials. n is the number of unit cells of NLO crystalline in the fundamental laser focal volume. Apart from the nonlinear coefficient, the number of unit cells of NLO crystalline play decisive roles in determining the η_{SHG}. In our case, due to the well-oriented arrangement of molecular packing, the dependence of η_{SHG} on the unit cell n could attribute to the thickness(L) of MMONS HMPs in the illuminated volume propagating along. In the transverse cross-section of HMP, there is a simple linear geometrical function of $L \propto d$ in our case. Herein, we could also choose edge length of the transverse cross-section of HMP in place of the number of unit cells n. According to the equation above, η_{SHG} should be proportional to d^2, in good agreement with the linear relationship with a slope of 2.01 ± 0.15 in Figure 3b. The maximum η_{SHG} = 8.3 ± 0.5% observed in MMONS HMPs is orders higher than those observed for surface SHG of GaP nanopillars and ZnTe nanowires, and is comparable to that

of β-BaB_2O_4 (known as BBO, a commercial NLO crystal) 2.2-μm microwire.[11]

Returning to Figure 2c, d, and e, when the fundamental laser was focused on one end (labelled as TIP-A) of a single HMP, SHG signal was not only observed at the pump point, bright SHG spot (labelled as TIP-B) was also observed at another end of HMP with much weaker signal from the body. This suggests that SHG light produced at TIP-A can be waveguided efficiently along the length direction of HMP and finally leaked at TIP-B. Note that such kind of waveguiding of SHG light was not observed in NLO nanofibers composed of 2,7-diphenyl-9H-fluoren-9-one (DPFO).[17]

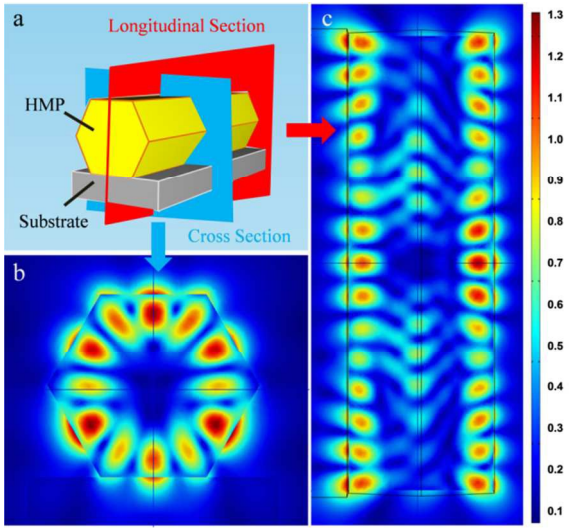

Figure 4. Optical mode simulations of the calculated $|E|^2$ field in of MMONS HMP.(a) The scheme of the model in FDTD simulations. (b) Cross-section views of the mode profile that are taken at the middle slice of the HMP cavity. (c) Standing wave pattern of the optical mode along the HMP axis. Red corresponds to the highest field density and blue is the lowest field density.

To understand the microcavity effect in MMONS HMPs, we calculated the local electric field $|E|^2$ distribution of 600-nm light in a MMONS HMP on quartz plate (refractive index n_{MMONS} = 1.8 and n_{quartz} = 1.3) by using the finite-difference time-domain (FDTD) method, with the side edges of the hexagonal cross section and the cavity length are 2.2μm and 12μm, respectively. Figure 4a is the scheme of the model in FDTD simulations. While the blue slice and red slice in Figure 4a is according to simulations result in hexagonal cross section(Figure 4b) and longitudinal section(Figure 4c), respectively. It can be seen from Figure 4b that nearly all the electric field $|E|^2$ intensities are limited inside the hexagon with near-field intensity aggregate at the inner surface of six edges of HMPs in hexagonal cross section. Simultaneously, standing wave pattern of the optical mode along the micro-prisms axis in longitudinal section is clearly showed in Figure 4c, and it is found that the mode profile is not much disturbed by the direct contact with the Substrate due the large interpolation in refractive index between MMONS HMPs and substrate. Simulations of MMONS HMPs above confirms typically helically propagating mode similar to InGaAs/GaAs nanopillars and InP nanowire,[32-34] both hexagonal prisms were reported recently. Therefore, the SHG light produced at one end of HMP can be coupled into WG photonic modes and propagates along the length of HMPs toward another end. The coupling efficiecy of SHG light into WG photonic modes is estimated according to $\eta_{WGM} = I_A/I_B$, in which I_A and I_B were recorded at TIP-A and TIP-B, respectively (Figure 2c-e). We found that η_{WGM} increases with increasing the wavelength of SHG light, for example, η_{WGM} = 50% and 80% for 525-nm and 600-nm SHG light, probably because the quality factor of WGM-cavity increases with increasing the wavelength.

To demonstrate the possibility of our MMONS HMPs in the use of photonic circuit, we constructed an optical interconnector by placing a MMONS HMP on the top of a microribbon of 1,3-diphenyl-2-pyroline (DP) (see the inset of Figure 5a). It had been reported that DP micro-ribbons exhibited excellent active waveguiding behavior. Figure 5a shows the FDTD calculation of the local electric field $|E|^2$ distribution of 600-nm light at the contact region between MMONS HMP and DP micro-ribbon as marked as C in the inset. It can be seen that SHG light guided through helically propagating WGM in MMONS HMP could be coupled into DP micro-ribbon at the contact region.

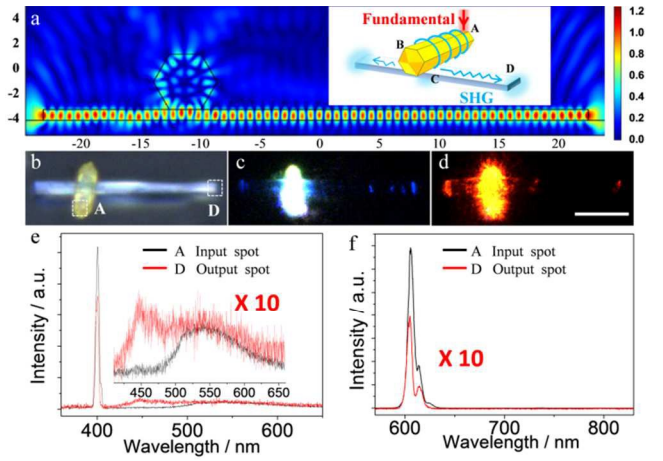

Figure 5. (a) Optical mode simulations of the calculated $|E|^2$ field in cross section of our photonic interconnector at the overlap spot C. Inset : Schematic illustration of designed photonic interconnector and the experimental setup used for testing; A:input spot; B: the other tip of HMP; C: overlap spot; D: output spot (right). (b) ~ (d) Bright-field microscopy image, images of 800nm and 1200nm focusing on A spot of the photonic interconnector respectively; scale bars: 15 μm. (e) and (f) Corresponding spectra of the input spot A (black curve) and output spot D (red curve) corresponding to those shown in (c)and (d).

Figure 5b shows the bright-field image of as-prepared optical interconnector, while Figure 5c and d are corresponding μ-PL images pumped at $\lambda_{fundamental}$ = 800 and 1200nm, respectively. The fundamental frequency laser beam was focused to a 1.5-μm -diameter spot on TIP-A, obviously, the blue-greenish (Figure 5c) and reddish (Figure 5d) μ-PL colors are observed at the input spot A and at the end of DP micro-ribbon (output spot D). Figure 5e depicts the μ-PL spectra recorded at the input spot A

(black) and output spot D (red) under conditions of $\lambda_{fundamental}$ = 800 nm. At the input spot A, 400-nm SHG signal was observed along with the MMONS PL at 520 nm (see black spectra in Figure 5e). Remarkably, besides SHG signal at 400 nm and MMONS PL at 520 nm, an additional PL band with a maximum at 450 nm was also observed at the output spot D (red spectra in Figure 5e), which is in good agreement with the PL spectrum of DP micro-ribbon (Figure S3b). Therefore, 400-nm SHG light coupled into DP micro-ribbon is re-absorbed by DP molecules, which then emit blue PL at 450 nm. In the case of $\lambda_{fundamental}$ = 1200nm (Figure5f), only 600-nm SHG light was observed at input spot A and output spot D. These results demonstrate that the helically propagating WGM of MMONS HMPs could be applied in the integration of on-chip photonic circuits.

Conclusions

In summary, we prepared single-crystalline MMONS HMPs via a liquid-phase self-assembly method. The SHG process is strongly polarization-dependent, related to the well-oriented dipole moments of MMONS molecules in HMPs. We found that the SHG efficiency (η_{SHG}) of MMONS HMPs increases with increasing the prism edge length (d) and reaches a maximum of η_{SHG} = 8.3 ± 0.5% for d =2.5 μm. WGM-like helically propagating mode cavity was confirmed in MMONS HMPs, which makes the local produced SHG light couple into the photonic modes and helically propagating along the length of HMPs with a relatively high coupling efficiency up to 80%. An optical interconnector is designed based on the unique helical propagation of SHG light, achieving multiple-wavelength effectual conversion by frequency doubling and spatially output by integrate with optical fiber. Furthermore, MMONS HMPs would be applied in the integration of on-chip and photonic circuits providing a possible way to accomplish frequency conversion with high efficiency and create coherent light for the frequencies where no alternative laser sources are available.

Acknowledgements

This work was supported by the National Natural Science Foundation of China (Nos. 21073200, 91222203, 21273251, 91333111, 21190034, 21221002), project of Construction of Innovative Teams and Teacher Career Development for Universities and Colleges Under Beijing Municipality (IDHT20140512), the National Basic Research Program of China (973) 2011CB808402, 2013CB933500, and the Chinese Academy of Sciences.

Notes and references

[a] Beijing Key Laboratory for Optical Materials and Photonic Devices, Department of Chemistry, Capital Normal University, Beijing 100190, P. R. China

[b] Beijing National Laboratory for Molecular Sciences (BNLMS), Institute of chemistry, Chinese Academy of Sciences, Beijing 100190, P. R. China

† Electronic Supplementary Information (ESI) available: [details of any supplementary information available should be included here]. See DOI: 10.1039/b000000x/

1 D. Cotter, *Science,* 1999, **286**, 1523-1528.
2 P. Yang, R. Yan, M. Fardy, *Nano Lett.,* 2010, **10,** 1529-1536.
3 R. Yan, D. Gargas, P. Yang, *Nat. Photon.,* 2009, **3**, 569-576.
4 S. Chu, G. Wang, W. Zhou, Y. Lin, L. Chernyak, J. Zhao, J. Kong, L. Li, J. Ren, J. Liu, *Nat. Nanotechnol.,* 2011, **6**, 506-510.
5 S. Gradečak, F. Qian, Y. Li, H.-G. Park, C. M. Lieber, *Appl. Phys. Lett.,* 2005, **87**, 173111.
6 B. Hua, J. Motohisa, Y. Kobayashi, S. Hara, T. Fukui, *Nano Lett.,* 2008, **9**, 112-116.
7 Marder, S. R.; Sohn, J. E.; Stucky, G. D. *Materials for Nonlinear Optics Chemical Perspectives*, **455**, American Chemical Society, Boston, MA, USA, 1991.
8 R. W. Boyd, *Nonlinear optics*, Academic press, 2003.
9 B. P. Mehl, R. L. House, A. Uppal, A. J. Reams, C. Zhang, J. R. Kirschbrown, J. M. Papanikolas, *J. Phys. Chem., A,* 2009, **114**, 1241-1246.
10 J. Long, B. Simpkins, D. Rowenhorst, P. Pehrsson, *Nano Lett.,* 2007, **7**, 831-836.
11 G. Qu, Z. Hu, Y. Wang, Q. Yang, L. Tong, *Adv. Funct. Mater.*, 2013, **23**, 1232-1237.
12 F. Dutto, C. Raillon, K. Schenk, A. Radenovic, *Nano Lett.,* 2011, **11**, 2517-2521.
13 J. Richter, A. Steinbruck, M. Zilk, A. Sergeyev, T. Pertsch, A. Tunnermann, R. Grange, *Nanoscale,* 2014, **6**, 5200-5207.
14 Y. S. Zhao, H. Fu, A. Peng, Y. Ma, Q. Liao, J. Yao, *Acc. Chem. Res.,* 2009, **43**, 409-418.
15 J. Clark, G. Lanzani, *Nat. Photon.,* 2010, **4**, 438-446.
16 Z. Xu, Q. Liao, Q. Shi, H. Zhang, J. Yao, H. Fu, *Adv Mater.,* 2012, **24**, OP216-OP220.
17 J. Xu, S. Semin, D. Niedzialek, P. H. Kouwer, E. Fron, E. Coutino, M. Savoini, Y. Li, J. Hofkens, I. H. Uji, D. Beljonne, T. Rasing, A. E. Rowan, *Adv Mater.,* 2013, **25,** 2084-2089.
18 D. Isakov, E. de Matos Gomes, M. S. Belsley, B. Almeida, N. Cerca, *Nanoscale,* 2012, **4**, 4978-4982.
19 J. Bierlein, L. Cheng, Y. Wang, W. Tam, *Appl. Phys. Lett.,* 1990, **56**, 423-425.
20 S. Tan, A. K. Bhowmik, S. Sodah, M. Thakur, *Appl. Phys. Lett.* 2000, **77**, 827
21 W. Tam, B. Guerin, J. C. Calabrese, S. H. Stevenson, *Chem. Phys. Lett.,* 1989, **154**, 93-96.
22 H. Fu, D. Xiao, J. Yao, G. Yang, *Angew. Chem. Int. Ed.,* 2003, **42**, 2883-2886.
23 W. Chen, H.-B. Fu, J.-N. Yao, *Chem. J. Chin. Univ.,* 2010, **3**, 030.
24 Q. Kong, Q. Liao, Z. Xu, X. Wang, J. Yao, H. Fu, *J. Am. Chem. Soc.,* 2014.
25 Q. Liao, H. Fu, C. Wang, J. Yao, *Angew. Chem.,* 2011, **50**, 4942-4946.
26 P. Munshi, B. W. Skelton, J. J. McKinnon, M. A. Spackman, *CrystEngComm,* 2008, **10**, 197-206.
27 J. E. Reeve, H. L. Anderson, K. Clays, *Phys. Chem. Chem. Phys.,* 2010, **12**, 13484-13498.
28 C. Wang, T. Zhang, W. Lin, *Chem. Rev.,* 2011, **112**, 1084-1104.
29 J. W. Park, H.-k. Hong, K.-S. Lee, C. S. Yoon, *Cryst. Growth Des.,* 2006, **6**, 2011-2020.
30 Q. Liao, H. Fu, J. Yao, *Adv Mater.,* 2009, **21,** 4153-4157.
31 Rachel G, Gerald B, Michael K, Anton S, Jessica R, Christian L, Wolfgang F, Andrey L, Werner P, Franz-Josef T, Thomas P, Andreas T, and Silke C, *Nano Lett.,* 2012, **12**, 5417.
32 R. Chen, T.-T. D. Tran, K. W. Ng, W. S. Ko, L. C. Chuang, F. G. Sedgwick, C. Chang-Hasnain, *Nat. Photon.,* 2011, **5**, 170-175.
33 J. Wiersig, *Phys. Rev. A,* 2003, **67**, 023807.
34 Wang, Z.; Tian, B.; Paladugu, M.; Pantouvaki, M.; Le Thomas, N.; Merckling, C.; Guo, W.; Dekoster, J.; Van Campenhout, J.; Absil, P.; Van Thourhout, D., *Nano Lett.,* 2013**, 13** (11), 5063-9.

